Analysis of end-winding proximity losses
in a high-speed PM machine

ADRIAN MLOT[1], MARIAN LUKANISZYN[1], MARIUSZ KORKOSZ[2]

[1]*Opole University of Technology*
Faculty of Electrical, Control and Computer Engineering
Gen. K. Sosnkowskiego, 3145-272 Opole
e-mail: a.mlot@po.opole.pl, m.lukaniszyn@po.opole.pl

[2]*Rzeszow University of Technology,*
Faculty of Electrical and Computer Engineering
Wincentego Pola 2, 35-959 Rzeszów
e-mail: mkosz@prz.edu.pl

Abstract: This paper presents a finite element investigation into the proximity losses in a high-speed permanent magnet (PM) machine for traction applications. A three-dimensional (3D) finite element analysis (FEA) is employed to evaluate and identify the end-winding contribution into the overall winding power loss generated. The study is focused on the end-winding effects that have not been widely reported in the literature. The calculated results confirm that the end-winding copper loss can significantly affect the eddy-current loss within copper and it should be taken into account to provide reasonable prediction of total losses. Several structures of the end-winding are analyzed and compared in respect to the loss and AC resistance. The results clearly demonstrate that the size of the end-winding has a significant impact on the power loss. The calculated results are validated experimentally on the high-speed permanent magnet synchronous machine (PMSM) prototype for selected various winding arrangements.

Key words: end-winding, permanent magnet motor, eddy-currents losses, proximity losses

1. Introduction

Main power loss sources within a high-speed permanent magnet synchronous machine are the winding, iron and magnets. In this paper, the authors focus on the end-winding AC power loss caused by eddy currents. The end-winding region is exposed to the flux patterns that are different from those within the winding active length. Most of the research has been focused on the proximity effects on the conductors placed into the slots [1-14]. Less attention has been paid to an influence of end-winding dimensions and size on the phenomena that contribute to the total eddy-current losses. In the presented machine prototype, the proximity effect is

significant and has to be precisely analyzed [3]. The stator winding power loss generated in a PM machine can be defined by two basic components, DC and AC ones. The DC winding power loss component and its thermal dependence is well understood and commonly used when estimating the machine performance. The AC winding power loss caused by magnetic fields generated by nearby conductors is more troublesome due to the complexity of the problem with various effects to be accounted for [1-3]. Those AC power loss components are present in any PM machine and their severity strongly depends on a particular machine design.

The analysis is limited to a three-tooth segment stator assembly owing to the symmetry and antisymmetry conditions, which reduces computational burden for the used FEA. The 3D FEA is employed to evaluate and identify the end-winding power loss contribution into the overall winding loss generated. Some guidelines regarding the FEA for the AC winding loss are given. Winding arrangements utilizing various conductor profile sizes and shapes of the end-winding are investigated to give more generic insight into the AC winding losses phenomena.

Experimental data are obtained to verify the theoretical predictions and demonstrate the difficulty of AC power loss analysis at high-speed operation. Some comments and recommendations regarding the end-winding construction are made.

2. Prototype high-speed PM motor and winding arrangements

The study is applied to the highly efficient (97% peak efficiency) and compact (2 kW/kg continuous rated) water jacket cooled PM motor designed for a large vehicle application. The prototype motor was designed to operate at high-speed up to 12000 rpm in order to minimize the overall system weight. The motor comprises 8 poles and 12 slots with a double layer concentrated winding. A prototype of the three-tooth stator section was designed to demonstrate AC losses in the stator winding and stator core, Figs. 1a-b. The segmented stator core is cooled via outer water jacket and the laminated stator segments are made of 0.35 mm silicon iron (M300-35 A). In the original design a high copper packing factor is realized through the use of a multi-stranded parallel conductor arrangement. A three-tooth segment stator setup is chosen in the analysis allowing for various winding arrangements to be constructed and evaluated in a timely manner. The laminated stator core hardware comprises a three-tooth stator section with slot geometry identical to that of the complete machine, Figs. 1b-c.
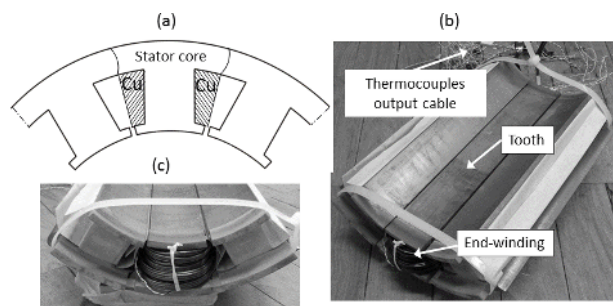

Fig. 1. Outline of the high-speed PM machine laminated stator core section (a), prototype of three-tooth stator section with a single tooth wound (b), and end-winding view (c)

To investigate the AC copper loss effects at high-speed operation three winding arrangements are constructed, Fig. 2a. Winding versions I and II are selected to demonstrate how important is to accurately build a 3D FE model of the winding conductors. And winding version III is used to investigate the influence of the geometry/size of end-winding on AC power loss. The baseline configuration, winding version I is representative of mush winding wound 'in hand' and comprising 7 parallel conductors with 16 turns and a 50% copper fill factor. The arrangement between turns with parallel wires ($\varnothing$1.6 mm) is not defined (randomly placed within the stator slot), and very difficult to be accurately represented in the FEA. Such a winding construction provides short and compact end-winding resulting in low end-winding DC resistance. However, the end-winding conductors are in the close proximity of the stator/teeth periphery being exposed to end effects.

Winding version II was wound using a custom manufactured multi-stranded bundle with conductors being bonded together. This allows for the conductor position within the stator slot together with bundle outer shape to be well defined and allowing for accurate model representation in the FEA. The winding consists of 14 turns with adjacent 7 parallel conductors ($\varnothing$1.6 mm) within a bundle and 44% copper fill factor. Fig. 2b shows the process of preparing 7 parallel bonded copper conductors as a turn which comprises a vertical strip of 4 conductors adjacent to a vertical strip of 3 conductors, and these two layers are glued together. Finally, an individual turn is arranged in precise location in the slot with respect to each other, Fig. 2c.

The winding version III comprises 10 turns of a solid conductor (10.25 mm $\times$ 1.30 mm) with rectangular cross-section with the 7% copper fill factor. This winding construction with the low value of the fill factor allows for various end-winding arrangements (including conductor profile sizes and shapes) to be investigated in a timely manner both experimentally and using the FEA.
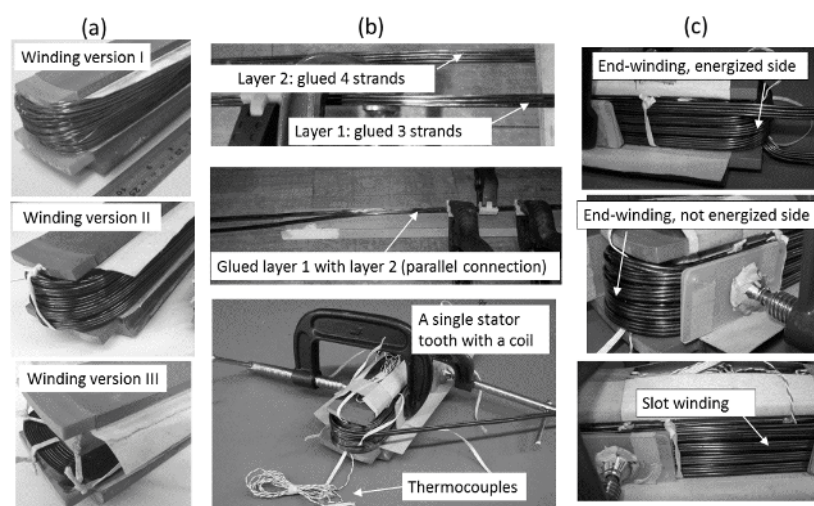

Fig. 2. Analyzed winding arrangement (a), and the process of making multi-stranded bundle with conductors being bonded together (b) with the final manufactured winding version II (c)

3. Experimental setup

Several winding versions were selected to measure the total DC and AC power loss using a power analyzer together with a precision current transducer. The DC and AC power losses are measured within the three-tooth segmented stator assembly. A voltage source inverter was used to supply a variable current to the tested winding, Fig. 3a.
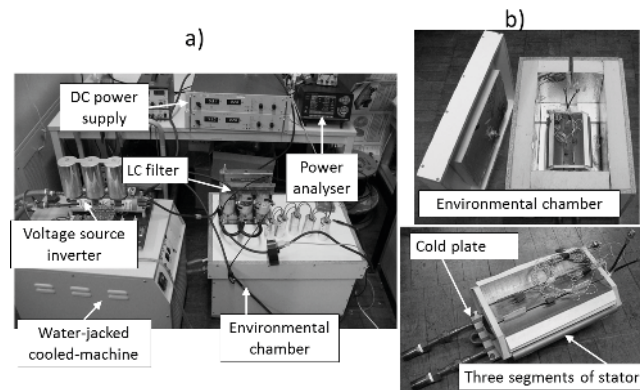

Fig. 3. Test bench for power loss and the temperature measure (a), and the three-tooth segment stator assembly with an environmental test chamber (b)

To emulate the water jacket assembly present in the complete machine, the three-tooth segment stator setup was mounted on a liquid-cooled cold plate using an interfacing plate, Fig. 3b. The cold-plate temperature was set to 20°C and controlled by a chiller unit assuring consistent measuring conditions. To provide good heat transfer between the laminated stator core, interfacing and cold plate, a thermal paste is used. A single tooth winding is instrumented with a number of type-K thermocouples. The environmental chamber is used as an enclosure to keep constant environmental conditions such as a fix temperature on the tested stator with a coil. Temperature measurements are monitored at each side of the coil including active length and end-windings at several excitation currents and frequencies.
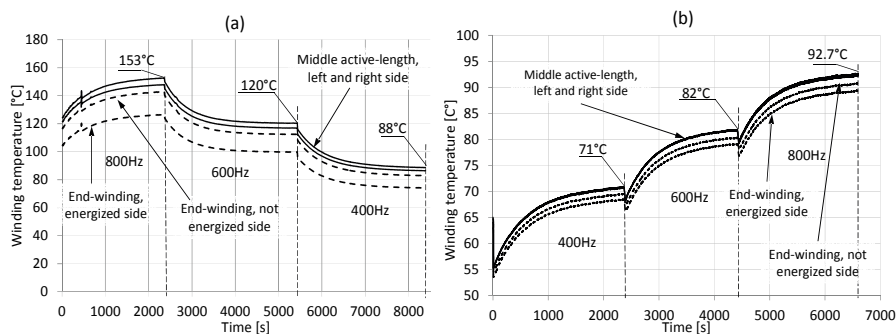

Fig. 4. Winding temperatures recorded for winding versions II (a) and III (b) at $I = 40$ A, the frequency ranges are 400 Hz, 600 Hz and 800 Hz

The thermal test for a single excitation point is carried until thermal equilibrium is reached. The thermal steady state is defined as temperature changes lower than 1°C over 10 min. The example of temperatures recorded for winding versions II and III at $I = 40$ A for various frequencies are demonstrated in Fig. 4. In both cases, lower copper temperatures can be seen at the energized side of the end-winding compared with the opposite side. Also, smaller temperature difference can be seen between both sides of the winding active-length.

4. Finite element models

Modeling of the end region of the machine requires a 3D program that solves Maxwell's equations and is not simple to investigate due to the complexity of the geometry and the difficulty of analysis [21]. In addition, the complexity is magnified due to the mesh discretization problem related to each winding strand. Analysis of the loss distribution within the three-tooth segment stator is carried out using the well-established discrete time step finite element method (FEM), with 3D formulations. Complete loss predictions including both the winding and the laminated stator core is required in order to separate the power loss components from measurements. Fig. 5 presents the geometry of the three-tooth laminated stator core with wound coil assumed in the FE calculations. Due to symmetry, the 3D model includes a half of the geometry, Figs. 5a-b. The yoke flux leakage caused by the air-gap between stator segments (here, 0.56 mm), indicated in Figs. 5a-b, is crucial for accurate loss prediction and therefore must be taken into account in the FE models.
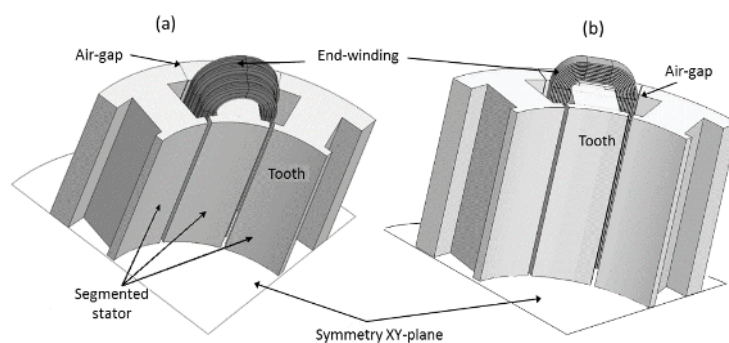

Fig. 5. 3D FE model representation of the three-tooth stator assembly with winding versions II (a) and III (b)

The laminated stator core's winding conductors are represented as separate solid conductors linked together via an external circuit and supplied from a sinusoidal current AC source, Fig. 6. It is important to note that each individual conductor within a bundle needs to be represented in the external circuit in order to provide correct power loss predictions [16]. A simplification making use of the grouped regions representing the individual bundles rather that individual conductors is incorrect here and would result in significant overestimation of the generated AC winding loss.
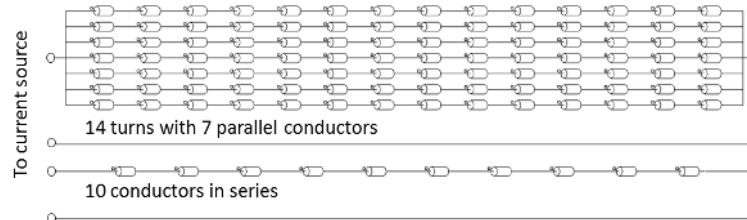
Fig. 6. Conductors' arrangements for the external circuit used in the FEA

Fig. 7 shows two different shapes of the end-winding of winding version III, which can affect the AC proximity effects. Case I shows the end-winding bonded in 90 deg. with semicircular shape in the corner, and the variable parameter *l* represents the horizontal length of end-winding (h_1 parameter varies with *l*). And the *l* parameter ranges from 2 mm to 32 mm and h_1 from 15.5 mm to 0.7 mm. Case II presents the rectangular shaped cross-section of the end-winding with the variable parameter h_2 representing the distance between the end-winding and stator core. The parameter h_2 ranges from 2 mm to 32 mm. It has to be noticed that this investigation of cases I and II leads to increase in the length of turns which affects the DC and AC copper losses. The arrangement of the conductors is depicted in Fig. 7c.
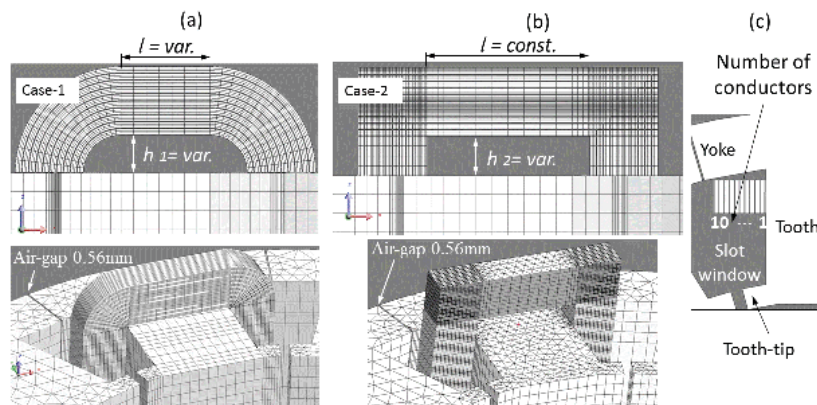

Fig. 7. 3D FE model with mesh discretization of the selected end-winding shapes for winding version III, semicircular shape (a) and rectangular shape (b), and conductors number definition (c)

5. AC loss analysis

It is impossible to extract the laminated stator core's losses experimentally by simple tests, since only the total loss measurements are available. Hence, to validate the theoretical findings an estimation of iron loss is needed. Computational methods for those losses have been widely described [4, 5, 7, 18, 19, 20]. The mean value of the iron loss in the laminated core pack based on the Bertotti formula has been calculated for harmonic excitation (the integral value of loss is calculated over the stator core volume) [21]. The stator core losses can be decom-

posed into the losses by hysteresis, the eddy currents losses, and the losses in excess as shown by expression (1), respectively.

$$P_{Fe} = \left[k_h \cdot B_m^2 \cdot f + \frac{\pi \cdot \sigma \cdot d^2}{6} \left(B_m \cdot f \right)^2 + k_e \left(B_m \cdot f \right)^{3/2} \cdot 8.67 \right] k_f \,, \tag{1}$$

where k_h, k_e, σ, d, f, B_m are the coefficients of losses by hysteresis, of losses in excess, the conductivity of the material (representing classical eddy current losses), the thickness of the lamination, the frequency and the peak value of the magnetic flux density, respectively. Material coefficients used for the iron loss predictions are listed in Table 1.

Table 1. Iron loss coefficients for a steel sheet M300-35 A

Hysteresis loss coefficient (k_h)	$W \cdot s \cdot T^{-2} \cdot m^{-3}$	93.89
Classical loss coefficient (σ)	$S \cdot m^{-1}$	2.22e6
Loss in excess coefficient (k_e)	$W(T \cdot s^{-1})^{-3/2} \cdot m$	1.33
Fill factor (k_f)	–	0.98
Thickness of steel iron (d)	m	3.5e-3

The AC copper loss within the solid conductors is determined from the Joule loss, and the AC proximity effects are accounted for both the active length and end-winding regions. The AC resistance increases under AC excitation as compared to DC operation. The ratio of AC resistance to DC resistance R_{AC}/R_{DC} is the commonly used figure of merit when assessing the high frequency effects. To account for the temperature variation in the loss prediction, the electrical resistivity is adjusted accordingly, then the copper loss from the Joule loss can be expressed by:

$$P_{Cu} = \rho_0 \left(1 + \alpha (T - 20^\circ C) \right) \int_V J^2 dV \,, \tag{2}$$

where, ρ_0 is the electrical resistivity $1.68 \cdot 10^{-8} \Omega m$ of copper at $20^\circ C$, T is the temperature at the operating point, J is the current density, and the temperature coefficient of resistivity α for copper is $93 \cdot 10^{-3} K^{-1}$.

Table 2 compares experimental results with FEM calculations of iron loss (P_{Fe}) and copper loss (P_{Cu}) for the winding versions I and II under AC current supply 40 A at 400 Hz, where the winding operating temperatures for copper was 73°C and 88°C, respectively. Under DC operating condition at 40 A the power loss for the same winding versions was measured and computed at working temperatures 57°C and 50.2°C, respectively.

Unsurprisingly, winding version II gives more accurate knowledge of a total AC power loss and it can be concluded that each position of conductor has to be well defined in the FEM. Nevertheless, the FEA results are still slightly overestimated as compared with measurements. The difference is mainly caused by the end-winding distance of designed coil, between conductors and stator tooth, which is much smaller compared with the FE model. Then it affects a power loss as shown in an example of winding version III (see Fig. 9). In the FE models the

same value of copper resistivity at the maximum measured winding temperature was used in the whole coil including the end-winding, whereas the temperature is quite different for both sides of the copper active-length and the end-winding (see Fig. 4), and this also affects the accurate copper loss prediction.

Table 2. Measured/calculated power losses and R_{AC}/R_{DC}

Winding version	AC and DC operating condition		Measurements	Calculations 3D FEA
I	Power loss ($P_{Cu} + P_{Fe}$)	AC, 400 Hz, 40 A$_{rms}$	54.4 W	inaccurate prediction[*]
		DC, 40 A	22 W	24 W
	Resistance ratio	R_{AC}/R_{DC}	2.47	n/a
II	Power loss ($P_{Cu} + P_{Fe}$)	AC, 400 Hz, 40 A$_{rms}$	61.5 W	68 W
		DC, 40 A	19.9 W	20.6 W
	Resistance ratio	R_{AC}/R_{DC}	3.1	3.3

*Caused by the arrangement between turns with parallel wires, which is not defined
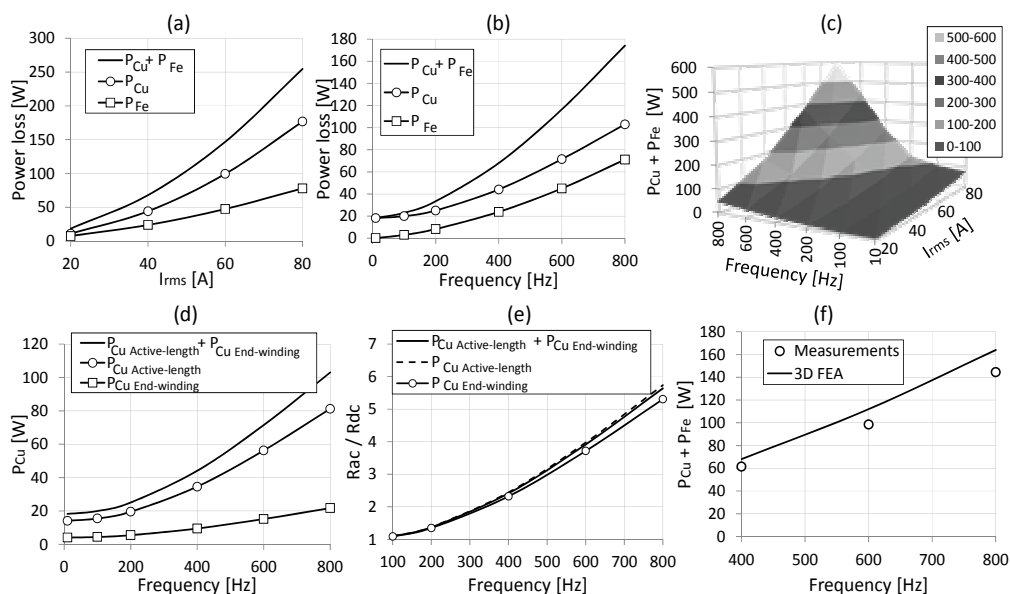

Fig. 8. Power loss results for winding version II at 20°C of winding temperature: vs. rms current at 400 Hz (a), vs. frequency at rms current 40 A (b), vs. rms current and frequency (c), vs. copper loss in slot and end-winding region at 40 A (d); and ratio R_{AC}/R_{DC} vs. frequency at 40 A (e), power loss measurements vs. frequency under 40 A at working winding temperature (f)

According to winding versions I and II, it is clear that defining positions of each conductor in FEM has a significant impact on the AC winding power loss predictions when considering multi-stranded winding design, in particular when a low number of turns per slot is considered [2, 16, 17]. Here, it is noticed that the multi-strand mush wound winding construction might

not be possible to be evaluated in an accurate manner when using the FEA due to a random position of the strands and undefined shape of the bundles. It was observed that randomly placed conductors generate less loss than the model with well known positions of conductors, caused by the temperature and winding fill factor difference which leads to change the heat transfer.
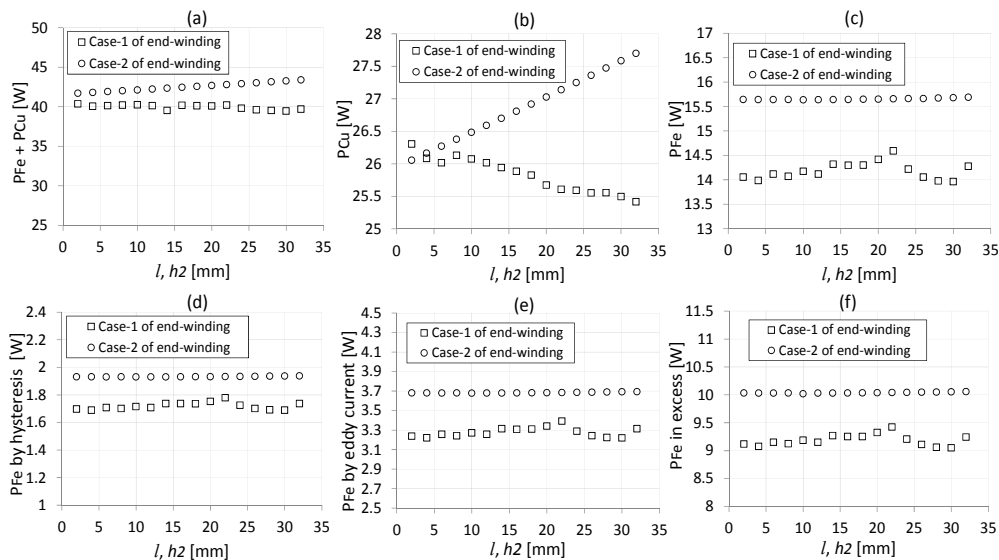

Fig. 9. Power loss vs. end-winding size parameters, investigation of winding version III: total power loss (a), total copper loss within the active-length and end-winding (b), iron loss (c), iron loss contribution: hysteresis loss (d), eddy current loss (e) and excess losses (f), results obtained at 40 A, 400 Hz

Power loss investigation for winding version II is depicted in Fig. 8. Fig. 8a-c presents the total power loss ($P_{Cu} + P_{Fe}$) changes versus AC current at 400 Hz, vs. frequency at 40 A, and vs. frequency and AC current, respectively. Also, separate copper loss vs. frequency at 40 A computed in the slot ($P_{Cu\ Active-length}$) and in the end-winding ($P_{Cu\ End-winding}$) is shown in Fig. 8d. This AC loss determines the increase of the resistance under AC excitation (R_{ac}), Fig. 8e. Figs. 8a-e regards to cold machine and Fig. 8f shows the measurements compared with FEA at working temperature (see Fig. 4a).

The 3D FEA of copper losses in the designed bar conductors, version III, was selected to investigate the end-winding size influence on the AC loss. For the end-winding case I with low h_1, smallest differences of AC power loss between measurements and 3D FEA have been found (that geometry is more close to the end-winding shape of the designed winding version III). The case II of end-winding shows a worse agreement with measured values of AC power loss, which may result from incorrect 3D modeling of end-windings. As shown in Fig. 9, end-winding size affected both copper and iron losses. Also, the separation of the iron loss in hysteresis, eddy current and the excess losses contributions is shown in Figs. 9d-f.

Fig. 10 shows the non-uniform current distributions of the current density in each conductor of the coil. The greatest proximity effect is recorded in the conductors that are placed

near the slot opening and in the conductors placed close to the stator core (where h_1 and h_2 is smallest). Both cases of end-winding shape with highest distances of h_1 and h_2 offer lowest current density recorded in the conductors.
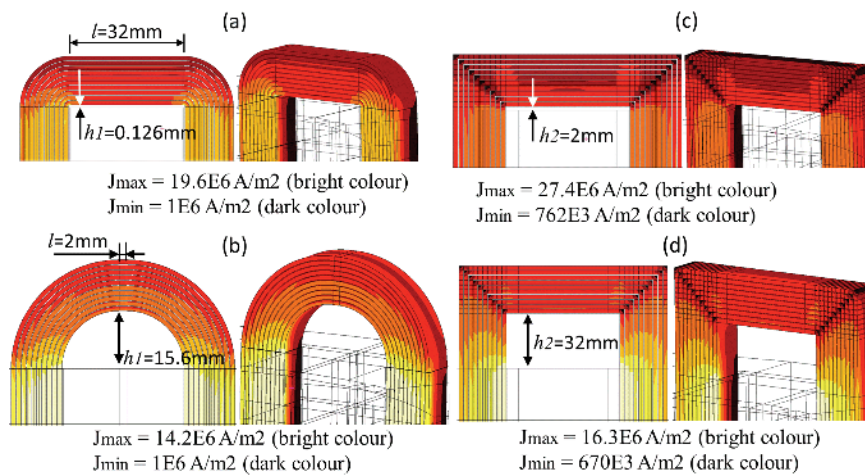

Fig. 10. Current density distribution within the conductors for end-winding case I (a-b) and case II (c-d) at 600 Hz, 40 A

From Fig. 10, it can also be concluded that one of the principal leakage flux components that has an impact on the iron and copper losses is the end-winding leakage flux [22-24], which is expected to be low when the end-winding is short and/or is located at high distances h_1 and h_2.

Very often coil failures occur in conductors located at the top of the coil closest to the slot opening or closest to the slot corners where the flux leakage is significant [2]. And one of the conductors failure reasons is increased AC resistance due to high frequency operation. To demonstrate the difference of AC loss in the strands the conducting regions were split into individual elements, and then AC to DC resistance ratio in the separate conductors was computed for both end-winding cases I and II of the winding version III, Fig. 11. For each case of end-winding shape two examples were demonstrated with smallest and highest distances between end-winding and stator core. Figs. 11a-c show the R_{AC}/R_{DC} ratio computed in the slot and end-winding as a sum. And Figs. 11b-d show the same resistance ratio just in the end-winding conductors. It can be seen that the proximity loss is quite different in each conductor depending on the position in the slot. It was also found that the conductors placed in the middle of the slot generate lowest R_{AC}/R_{DC}. For example, the R_{AC}/R_{DC} is 1.95 in conductor placed nearest the slot corner (conductor No.1, see Fig. 7c), and it was reduced to 1.48 in the conductor placed in the middle of the slot (conductor No. 11, see Fig. 7c). Also, the end-winding conductors placed nearest the stator core armature generate more eddy-currents than the other ones, Fig. 11b. Higher R_{AC}/R_{DC} can have a substantial effect on the cooling system and create hot spots.
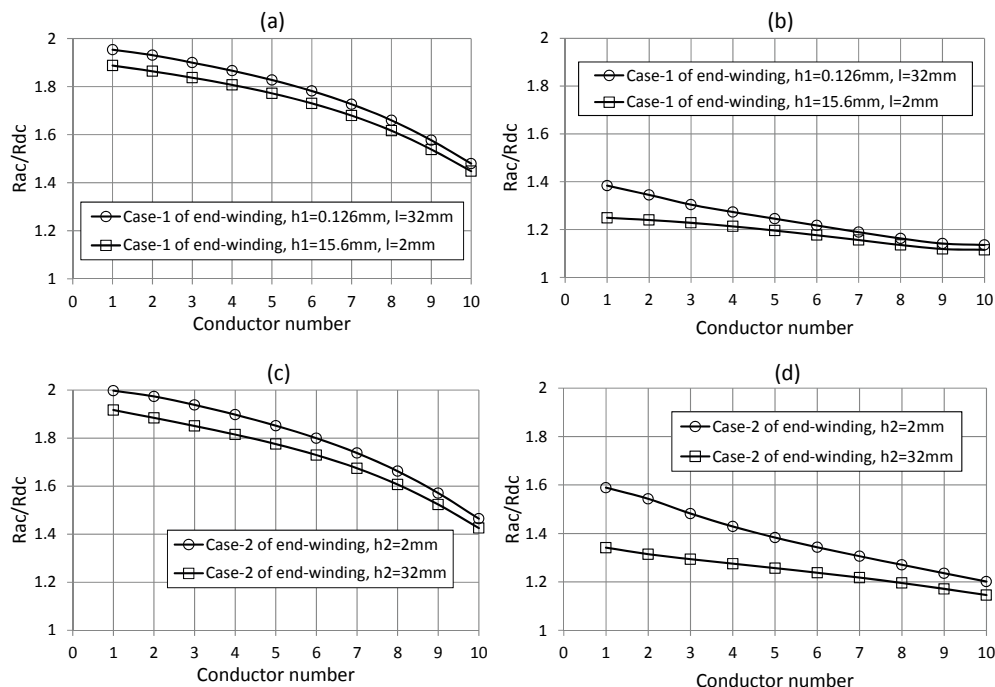
Fig. 11. The AC to DC resistance ratio for winding version III in each conductor at 600 Hz and 40 A. The R_{AC}/R_{DC} resistance of end-winding case I computed in the slot and end-winding (a) and in the end-winding only (b) and the R_{AC}/R_{DC} resistance of end-winding case II computed in the slot and end-winding (c) and in the end-winding only (d)

6. Conclusion

The analysis of the proximity losses in the end-windings have clearly shown that the power loss prediction at the AC operation is a complex task and the end connection should be properly designed and calculated. Both proximity and skin effects in a motor winding can be difficult to compute accurately because they are a function of conductor's geometry, winding layout and frequency. Also, it strongly depends on stator/rotor core and PM geometry. Some of these factors here have been selected to illustrate the AC losses.

Winding arrangements utilizing various conductor profile sizes and shapes of the end-winding have been investigated to give more generic insight into the AC winding losses phenomena. The end connection portion in this particular machine significantly contributes to the copper and iron losses. Depending on end-winding size/shape, the power loss in the armature core (P_{Fe}) and copper (P_{Cu}) ranges between 13.7-15.6 W and 25.4-27.5 W, respectively. To demonstrate the importance of the effect of winding ends on the copper loss, the analysis of eddy-currents has been performed within the slot ($P_{Cu\ Active-length}$) and end-winding ($P_{Cu\ End-winding}$) separately. It has been found that placing conductors nearest the tooth and placing end-winding conductors nearest the stator core leads to higher AC to DC resistance ratio.

The theoretical prediction has been compared against experimental data showing good correlation. It has been shown that the AC power loss prediction requires to build an accurate FE model with defined positions of each individual conductors within the slot, which is more complex when windings consist of more conductors with a low number of turns.

References

[1] Iwasaki S., Deodhar R.P., Liu Y., Pride A., Zhu Z.Q., Bremner J.J., *Influence of PWM on the proximity loss in permanent-magnet brushless AC machines*, IEEE Transactions on Industry Applications 45(4): 1359-1367 (2009).

[2] Mlot A., Korkosz M., Grodzki P., Lukaniszyn M., *Analysis of the proximity and skin effects on copper loss in a stator core*, Archives of Electrical Engineering 63(2): 211-225 (2014).

[3] Wrobel R., Mlot A., Mellor P.H., *Investigation of end-winding proximity losses in electromagnetic devices*, XIX International Conference on Electrical Machines, Rome, 1- 6 (2010).

[4] Cheng K.W.E., Evans P.D., *Calculations of winding losses in high-frequency toroidal inductors using single strand conductors*, IEE Electric Power Applications 141: 52-62 (1994).

[5] Sippola M., Sepponen R.E., *Accurate prediction of high-frequency power-transformer losses and temperature rise*, IEEE Transactions on Power Electronics 17: 835-847 (2002).

[6] Spang M., Albach M., *Optimized winding layout for minimized proximity losses in coils with rod cores*, IEEE Transactions on Magnetics 44: 1815-1821 (2008).

[7] Shinagawa T., Suzuki T., Noda M., Shimura Y., Enoki S., Mizuno T., *Theoretical analysis of AC resistance in coil using magnetoplated wire*, IEEE Transactions on Magnetics 45: 3251-3259 (2009).

[8] Dowell P.L., *Effects of eddy currents in transformer windings*, Proceedings of the Institution of Electrical Engineers 113(8): 1387-1394 (1966).

[9] Kondrath N., Kazimierczuk M.K., *Inductor winding loss owing to skin and proximity effect including harmonics in non-isolated pulse-width modulated dc-dc converters operating in continuous conduction mode*, IET Power Electronics 3: 989-1000 (2010).

[10] Albach M., Rossmanith H., *The influence of air gap size and winding position on the proximity losses in high frequency transformers*, 32nd IEEE Annual Power Electronics Specialists Conference 3: 1485-1490 (2001).

[11] Evans P.D., Chew W.M., *Reduction of proximity losses in coupled inductors*, IEE Electronic Power Applications 138: 51- 58 (1991).

[12] Iwasaki S., Deodhar R.P., Yong L., Pride A., Zhu Z.Q., *Influence of PWM on proximity loss in permanent-magnet brushless AC machines*, IEEE Transactions on Industry Applications 45: 1359-1367 (2009).

[13] Anh-Tuan G., Meunier G., Chadebec O., Margueron X., Keradec J.P., *High-frequency proximity losses determination for rectangular cross-section conductors*, IEEE Transactions on Magnetics 43: 1213-1216 (2007).

[14] Thomas A.S., Zhu Z.Q., Jewell G.W., *Proximity loss study in high speed flux-switching permanent magnet machine*, IEEE Transactions on Magnetics 45: 4748-4751 (2009).

[15] Nakane H., Watanabe T., Nagata C., Fujiwara S., Yoshizawa S., *Measuring the temperature dependence of resistivity of high purity copper using a solenoid coil (SRPM method)*, IEEE Transactions on Instrumentation and Measurement 41: 107-110 (1992).

[16] Mircea P., Dorrell D.G., *Skin effect and proximity losses in high speed brushless permanent magnet motors*, IEEE Energy Conversion Congress and Exposition 3520-3527 (2013).

[17] Mircea P., Staton D.A., Dorrell D.G., *Study of the thermal aspects in brushless permanent magnet machine performance*, IEEE Electrical Machines Design Control and Diagnostics 60-69 (2013).

[18] Ionel D.M., Popescu M., Dellinger S.J., Miller T.J.E., Heideman R.J., McGlip M.I., *On the variation with flux and frequency of the core loss coefficients in electrical machines*, IEEE Transactions on Industry Applications 42: 658-667 (2006).

[19] Ionel D.M., Popescu M., McGlip M.I., Miller T.J.E., Dellinger S.T., Heideman R.J., *Computation of core losses in electrical machines using improved models for laminated steel*, IEEE Transactions on Industry Applications 43: 1554-1562 (2007).

[20] Zhao H., Luo Y., Ren Y., Peter B., *A complete model for iron losses prediction in electric machines including material measurement, data fitting*, FE computation and experimental validation, Przeglad Elektrotechniczny 5b: 52-56 (2012).

[21] Cedrat Ltd, France, http://www.cedrat.com.

[22] Spooner E., Williamson A.C., Catto G., *Modular design of permanent-magnet generators for wind turbines*, IEE Proceedings – Electric Power Applications 143: 388-395 (1996).

[23] Zhang W., Wu X., Wang D., *Influence of stator end-winding structure on the end-winding leakage inductance with method of vector-potential*, International Conference on Electrical Machines and Systems (ICEMS), pp. 3274-3277 (2014).

[24] Bartolozzi M., Tessarrolo A., Bruzzese C., *Analytical computation of end-coil leakage inductance of round-rotor synchronous machines field winding*, IEEE Transactions on Magnetics (52)2:1-9 (2015).